



# Structural applications of the combined finite–discrete element method

Ante Munjiza<sup>1</sup> · Hrvoje Smoljanović<sup>1</sup> · Nikolina Živaljić<sup>1</sup> · Ante Mihanović<sup>1</sup> · Vladimir Divić<sup>1</sup> · Ivana Uzelac<sup>1</sup> · Željana Nikolić<sup>1</sup> · Ivan Balić<sup>1</sup> · Boris Trogrlić<sup>1</sup>

Received: 10 July 2019 / Accepted: 26 September 2019 / Published online: 4 October 2019  
© OWZ 2019

## Abstract

This aim of this paper is to present the application of the combined finite–discrete element method (FDEM) in structural mechanics. FDEM is an innovative numerical technique, which has been intensively used in the past several decades in various engineering simulations. FDEM combines the advantages of both the finite and the discrete elements and enables the simulation of initiation and propagation of cracks, as well as interaction of a large number of discrete elements. The examples presented in this paper show the advantages of FDEM in the analysis of structural mechanics issues including dry-joint masonry structures, concrete and reinforced concrete structures, masonry structures with mortar joints and confined masonry structures, cable and truss structures, membrane structures, and plate and shell structures.

**Keywords** Combined finite–discrete element method (FDEM) · Numerical analysis · Structural mechanics

## 1 Introduction

With the rapid developments in the area of computer performance, complex structural design tasks can be reduced to a mathematical problem solved with the help of a numerical method. Finite element method (FEM) was the first widely accepted numerical method for structural analysis. Numerical models based on the finite element method treat a structure a priori as a continuum and, as a result, exhibit difficulties in describing the discontinuous nature of certain structural problems. This method was further extended to include the propagation of various discontinuities which resulted in the extended finite element method (XFEM). However, XFEM proved to be inadequate for problems with large deformations, significant mesh distortions and discontinuities. In the last two decades, meshfree methods have been intensively developed. These methods provide a solution using a set of randomly distributed nodes without the predefined elements linking the nodes. However, when dealing with a structural problem involving several, maybe even thousands of mutually interacting separate particles,

each of them should be treated as one discrete element. The latter problem resulted in the discrete element method (DEM), which, in combination with FEM, allows the contact interaction between discrete elements paired with large displacements, large rotations, deformability and, finally, the transition from continuum to discontinuum within each discrete element. The aim of this paper is to present the advantages of the combined finite–discrete element method in structural mechanics, which is an approach combining the benefits of the finite and discrete elements method.

## 2 Aspects of structural engineering in FDEM

Combined finite–discrete element method is intended for the dynamic analysis of a large number of mutually interacting discrete elements, where the elements can fracture and fragment, thus increasing the total number of discrete elements [1]. Within FDEM, each discrete element is discretised with its own finite element mesh, thus enabling the deformability of discrete elements. Fracture and fragmentation processes are also implemented within the finite element mesh. The mass of discrete elements is lumped into the nodes of finite elements, while the time integration of the motion equation is applied node by node and degree-of-freedom by degree-of-freedom. This is performed in explicit form by using the

✉ Ante Munjiza  
antoniomunjiza@outlook.com

<sup>1</sup> FGAG, University of Split, Split, Croatia

central difference time integration scheme. The contact forces resulting from the interaction process between two discrete elements are determined by the numerical representation of contact impact, which is executed by employing contact detection and contact interaction procedures [1–3].

### 2.1 Contact detection and interaction

A contact detection algorithm is aimed at detecting the pairs of mutually contacting discrete elements and eliminating the non-contacting pairs that are far apart. Munjiza-NBS contact detection algorithm is implemented in Y code based on FDEM [2]. The total CPU time required by this algorithm to detect all contacting pairs of discrete elements is proportional to the total number of discrete elements.

Once the contacting couples are detected by the contact detection algorithm, the contact interaction algorithm is applied to calculate the contact forces between them. The contact interaction between the discrete elements is calculated by using the distributed potential contact force based on the penalty function method [3] which is based on the assumption that two contacting bodies, one denoted as the contactor and the other as the target, penetrate into each other, thus generating a distributed contact force (Fig. 1). As the contactor penetrates an elemental volume  $dV$  into the target, it generates the infinitesimal contact force given by:

$$d\mathbf{f}_c = [\text{grad}\varphi_c(P_c) - \text{grad}\varphi_t(P_t)] dV \tag{1}$$

where  $P_t$  and  $P_c$  represent the points in which the target and the contactor overlap, while  $\varphi$  is a potential field assuming the zero-equaling value on the edge and the maximum value at the centre of the discrete element.

The total contact force exerted by the target onto the contactor is obtained by the integration of the infinitesimal contact force  $d\mathbf{f}_c$  over the overlap volume  $V$  (Fig. 6), which leads to:

$$\mathbf{f}_c = \int_{V=\beta_t \cap \beta_c} (\text{grad}\varphi_c - \text{grad}\varphi_t) dV \tag{2}$$

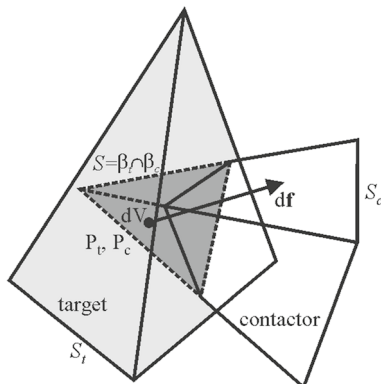


**Fig. 1** Contact force due to an infinitesimal overlap around points  $P_t$  and  $P_c$

The previous equation can also be written as an integral over the surface  $S$  of the overlapping volume as follows:

$$\mathbf{f}_c = \int_{S_{\beta_t \cap \beta_c}} \mathbf{n}(\varphi_c - \varphi_t) dS \tag{3}$$

It should be emphasised that each tetrahedron is considered twice: once as a contactor and once as a target.

Within the contact interaction algorithm, Coulomb-type law of friction is also implemented [4].

### 2.2 Fracture and fragmentation

There are several approaches to fracture and fragmentation in the numerical analysis. The early solutions were based on the smeared crack model. Later, these were substituted by the discrete crack model. The model adopted within FDEM is actually a combination of smeared and discrete crack approaches [5]. It was designed with the aim of modelling progressive fracture and failure including fragmentation and of creating a large number of rock fragments. For that purpose, the strain softening which appears in the material after reaching the tensile or shear strength is described in terms of displacement. The separation of the surfaces of the adjacent finite elements induces a bonding stress (see Fig. 2a) which is assumed as a function of the size of separation  $\delta$  (see Fig. 2b).

The area under the stress–displacement curve represents the energy release rate  $G_f = 2\gamma$ , where  $\gamma$  is the surface energy, i.e. the energy needed to extend the crack surface by a unit area. Theoretically, there is no separation  $\delta$  before reaching the tensile strength. In the actual implementation, it is enforced by the penalty method. For the separation  $\delta \leq \delta_c$ , the bonding stress is given by:

$$\sigma = \left[ \frac{2\delta}{\delta_t} - \left( \frac{\delta}{\delta_t} \right)^2 \right] f_t \tag{4}$$

where  $\delta_t = 2hf_t/p$  is the normal separation inducing the bonding stress equal to the tensile strength  $f_t$ ,  $h$  is the size of the

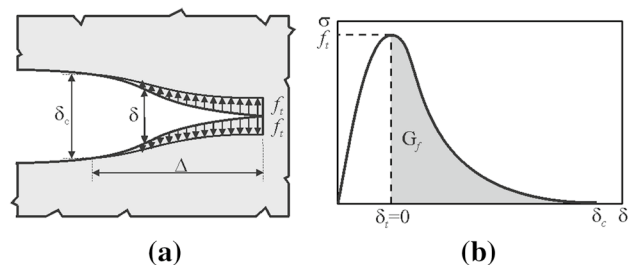


**Fig. 2** **a** Single crack model [5], **b** strain softening defined in terms of displacement [5]

finite element, and  $p$  is the penalty term. Hence, the relative displacement error is independent of the finite element size [6–8].

After reaching the tensile strength  $f_t$ , the stress decreases with an increase of the normal separation  $\delta$ , whereas at  $\delta = \delta_c$  the bonding stress tends to zero. For the separation  $\delta_t < \delta < \delta_c$ , the bonding stress is given by:

$$\sigma = z f_t \tag{5}$$

where  $z$  is the scaling function representing the softening behaviour of the concrete. According to Hillerborg [1], it is used for approximating the experimental stress–displacement curves for the concrete:

$$z = \left[ 1 - \frac{a + b - 1}{a + b} e^{D \frac{a+cb}{(a+b)(1-a-b)}} \right] [a(1 - D) + b(1 - D)^c] \tag{6}$$

where  $a = 0.63$ ,  $b = 1.8$  and  $c = 6.0$ , while the damage parameter  $D$  is determined according to the expression:

$$D = \begin{cases} (\delta - \delta_t) / (\delta_c - \delta_t), & \text{if } \delta_t < \delta < \delta_c; \\ 1, & \text{if } \delta > \delta_c \end{cases} \tag{7}$$

The same formulation can be used for other semi-brittle materials using appropriate parameters, as obtained by experimental research.

### 2.3 Trusses and cable structures in FDEM

The discretisation of cable and truss structures within 3D FDEM is performed by two-noded finite elements [9] as shown in Fig. 3.

Based on the length of the finite element in initial  $l_i$  and current  $l_c$  configuration (see Fig. 4a), the axial strain is obtained according to the following equation:

$$\epsilon = (l_c - l_i) / l_i \tag{8}$$

which, taking into account the linear viscoelastic material behaviour, yields the axial strain in the form of:

$$\sigma = E \epsilon + \bar{\mu} \dot{\epsilon} \tag{9}$$

where  $E$  represents the modulus of elasticity, while  $\bar{\mu}$  represents the damping coefficient. Axial forces acting in the

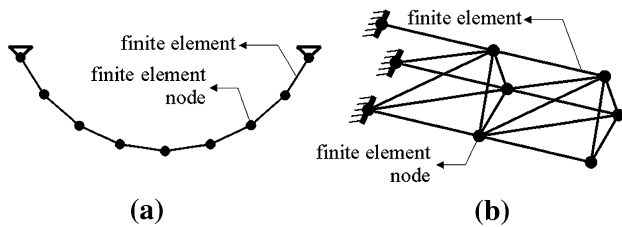


Fig. 3 Discretisation of: **a** cable structures, **b** truss structures

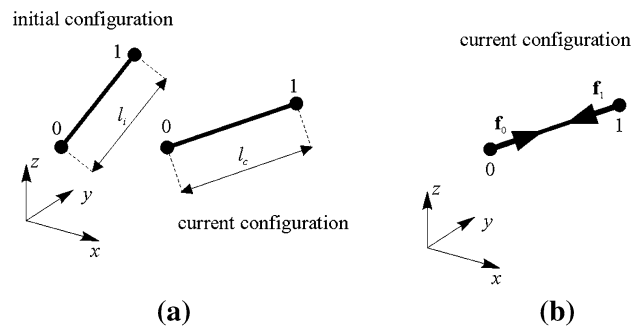


Fig. 4 Two-noded finite element: **a** initial configuration and current configuration, **b** forces in the finite element nodes due to deformation of the finite element

finite element nodes (see Fig. 4b) are obtained according to the equation:

$$f_0 = f_1 = \sigma A \tag{10}$$

where  $A$  is the area of the cross section.

This numerical scheme facilitates the introduction of aeroelastic damping as an external force, acting contrary to the relative motion of fluid and the structure. In the structures with large deflections, such as cable, truss and membrane structures, the aeroelastic damping is a significant dissipator of kinetic energy [9].

### 2.4 Frame structures in FDEM

The analysis of frame structures within FDEM is enabled by introducing the beam-type finite element and bending stiffness [10]. For that purpose, the finite element nodes are considered together with two adjacent nodes (see Fig. 5) defining a fictitious circle with curvature obtained according to:

$$\kappa = 2 \frac{\sin \varphi}{d} \tag{11}$$

Based on the change of the curvature between the current and the initial configuration  $\Delta\kappa$ , and by adopting the linear

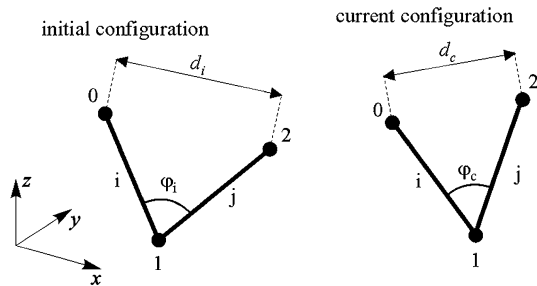


Fig. 5 Initial and current positions of observed node 1 with adjacent nodes 0 and 2

viscoelastic material behaviour, the moment  $m$  acting in the observed node 1 is obtained according to the equation:

$$m = EI\kappa + \mu \dot{\kappa} \tag{12}$$

where  $E$  represents the modulus of elasticity,  $I$  represents the moment of inertia of the cross section, while  $\mu$  represents the damping coefficient.

The bending moment  $m$  (see Fig. 6a) is finally transferred to the nodes of the finite elements  $i$  and  $j$  in the form of the pair of forces (see Fig. 6b) equalling:

$$\begin{aligned} f_{0i} = f_{1i} &= \frac{m}{l_i} \\ f_{1j} = f_{2j} &= \frac{m}{l_j} \end{aligned} \tag{13}$$

The forces resulting from the moment are then added to the nodal forces resulting from the axial bearing mechanism.

### 2.5 Membrane structures in FDEM

The discretisation of the membrane structures within FDEM is performed by three-noded triangular finite elements [11] transferring only the membrane stress, i.e. stresses in their plane. In order to improve the CPU efficiency while calculating the membrane stresses, a local coordinate system is adopted within each finite element, as shown in Fig. 7, where  $(\bar{x}, \bar{y}, \bar{z})$  represent the initial local Cartesian coordinates, while  $(\tilde{x}, \tilde{y}, \tilde{z})$  represent the current local Cartesian coordinates.

Based on the coordinates of nodes in the initial and the current configuration, the deformation gradient  $\mathbf{F}$  is obtained according to the equation:

$$\mathbf{F} = \begin{bmatrix} \tilde{x}_1 & \tilde{x}_2 \\ \tilde{y}_1 & \tilde{y}_2 \end{bmatrix} \begin{bmatrix} \bar{x}_1 & \bar{x}_2 \\ \bar{y}_1 & \bar{y}_2 \end{bmatrix}^{-1} \tag{14}$$

which yields the Green–St. Venant’s strain tensor  $\mathbf{E}$  according to:

$$\mathbf{E} = \frac{1}{2}(\mathbf{F}\mathbf{F}^T - \mathbf{I}) \tag{15}$$

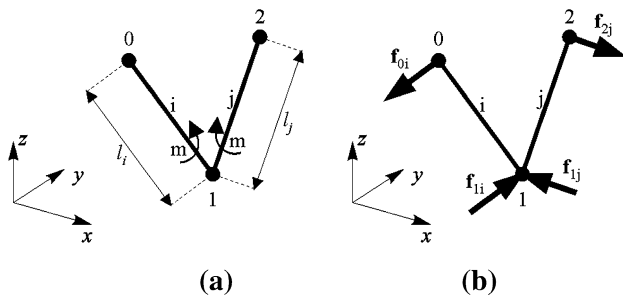


Fig. 6 Bending moment: **a** in finite element node; **b** in the form of equivalent nodal forces

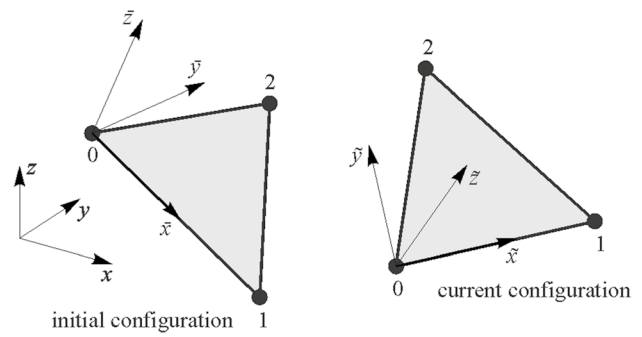


Fig. 7 Three-noded triangular finite element in initial configuration and current configuration

By adopting the linear viscoelastic material behaviour, the Cauchy’s stress tensor  $\mathbf{T}$  is obtained according to:

$$\mathbf{T} = \frac{E}{1 + \nu} \tilde{\mathbf{E}}_d + \frac{E}{1 - 2\nu} \tilde{\mathbf{E}}_s + \bar{\mu} \mathbf{D} \tag{16}$$

where  $E$  is the modulus of elasticity,  $\nu$  is the Poisson’s ratio,  $\tilde{\mathbf{E}}_d$  is the shape-changing part,  $\tilde{\mathbf{E}}_s$  is the volume-changing part of the Green–St. Venant’s strain tensor [1],  $\bar{\mu}$  is the damping coefficient, and  $\mathbf{D}$  is the rate of the strain tensor [1].

Traction forces over each of the edges of the triangular finite element (see Fig. 8a) are obtained according to the equation:

$$\mathbf{s} = \mathbf{T}\mathbf{n} = \begin{bmatrix} s_{\bar{x}} \\ s_{\bar{y}} \end{bmatrix} = \begin{bmatrix} t_{\bar{x}\bar{x}} & t_{\bar{x}\bar{y}} \\ t_{\bar{y}\bar{x}} & t_{\bar{y}\bar{y}} \end{bmatrix} \begin{bmatrix} n_{\bar{x}} \\ n_{\bar{y}} \end{bmatrix} \tag{17}$$

where  $n_{\bar{x}}$  and  $n_{\bar{y}}$  represent the components of the outer normal to the edges. Finally, the traction forces are transformed onto the nodes of finite elements in the form of equivalent nodal forces, where each node assumes half of the traction force of the corresponding finite element edge, as shown in Fig. 8b.

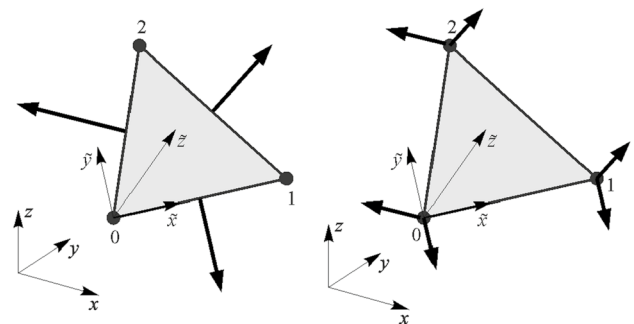


Fig. 8 Forces due to membrane stresses: **a** traction forces; **b** equivalent nodal forces

### 2.6 Plate and shell structures in FDEM

The analysis of plate and shell structures within FDEM is enabled by introducing the bending stiffness over the finite element edges within the numerical model for membrane structures [12–14]. In order to account for the bending-carrying capacity, the triangular finite elements are observed together with the three nodes of adjacent finite elements, as shown in Fig. 9.

The second-order polynomial in the local coordinate system is determined through six nodes in both the current

$$\bar{z} = \bar{\alpha}_1 + \bar{\alpha}_2\bar{x} + \bar{\alpha}_3\bar{y} + \bar{\alpha}_4\bar{x}\bar{y} + \bar{\alpha}_5\bar{x}^2 + \bar{\alpha}_6\bar{y}^2 \tag{18}$$

and the initial configuration

$$\tilde{z} = \tilde{\alpha}_1 + \tilde{\alpha}_2\tilde{x} + \tilde{\alpha}_3\tilde{y} + \tilde{\alpha}_4\tilde{x}\tilde{y} + \tilde{\alpha}_5\tilde{x}^2 + \tilde{\alpha}_6\tilde{y}^2 \tag{19}$$

which yields the change of the curvature within the finite element in the local coordinate system according to:

$$\kappa_{\bar{x}} = 2(\tilde{\alpha}_5 - \bar{\alpha}_5), \quad \kappa_{\bar{y}} = 2(\tilde{\alpha}_6 - \bar{\alpha}_6), \quad \kappa_{\bar{x}\bar{y}} = 2(\tilde{\alpha}_4 - \bar{\alpha}_4) \tag{20}$$

Considering the linear viscoelastic material behaviour, bending and twisting moments within the observed finite element are determined according to:

$$\begin{aligned} m_{\bar{x}} &= I(\kappa_{\bar{x}} + \nu\kappa_{\bar{y}}) + (\dot{\kappa}_{\bar{x}} + \nu\dot{\kappa}_{\bar{y}})\mu \\ m_{\bar{y}} &= I(\kappa_{\bar{y}} + \nu\kappa_{\bar{x}}) + (\dot{\kappa}_{\bar{y}} + \nu\dot{\kappa}_{\bar{x}})\mu \\ m_{\bar{x}\bar{y}} &= I(1 - \nu)\kappa_{\bar{x}\bar{y}} + (1 - \nu)\dot{\kappa}_{\bar{x}\bar{y}}\mu \end{aligned} \tag{21}$$

where  $\dot{\kappa}_{\bar{x}}$ ,  $\dot{\kappa}_{\bar{y}}$  and  $\dot{\kappa}_{\bar{x}\bar{y}}$  represent the velocity of the change in curvature,  $\mu$  represents the damping coefficient, while  $I$  represents the bending stiffness given by

$$I = \frac{Et^3}{12(1 - \nu^2)} \tag{22}$$

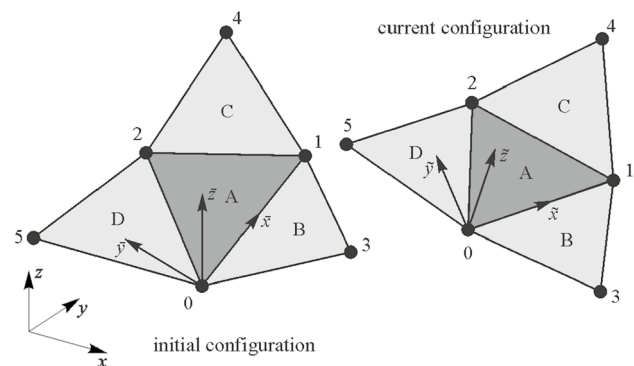


Fig. 9 Observed finite element A with adjacent finite elements B, C and D in initial configuration and current configuration

with  $t$  being the shell thickness. Equations (21) yield the bending moment  $m_{nA}$  (see Fig. 10a) along the corresponding side of the observed finite element according to the equation

$$m_{nA} = \frac{1}{2}(m_{\bar{x}}n_{\bar{x}} + m_{\bar{y}}n_{\bar{y}} + 2m_{\bar{x}\bar{y}}n_{\bar{x}}n_{\bar{y}}) \tag{23}$$

where  $n_{\bar{x}}$  and  $n_{\bar{y}}$  represent the components of the unit outer normal on the corresponding side of the finite element in the local coordinate system.

Bending moment  $m_n$  is subsequently converted into the equivalent nodal forces

$$\begin{aligned} f_2 &= \frac{m_{nA}l}{h_A}, \quad f_{0A} = f_2 \frac{l_{A2}}{l}, \quad f_{1A} = f_2 \frac{l_{A1}}{l} \\ f_3 &= \frac{m_{nA}l}{h_A}, \quad f_{0B} = f_3 \frac{l_{B2}}{l}, \quad f_{1B} = f_3 \frac{l_{B1}}{l} \end{aligned} \tag{24}$$

perpendicular to the plane of the observed finite element A and the adjacent finite element B, as shown in Fig. 10b.

This procedure is repeated for each side of the observed finite element and subsequently for each finite element. The forces resulting from the moment are then added to the nodal forces resulting from the membrane carrying mechanism.

### 2.7 Reinforced concrete structures in FDEM

For the purpose of analysing the reinforced concrete structures [15–17], the original Y-FDEM programme package was extended with a reinforcing bar finite element and a reinforcing bar contact element simulating the behaviour of the reinforcing bar (see Fig. 11). The reinforcing bar finite elements are implemented within the concrete finite elements and simulate the behaviour of the reinforcing bar

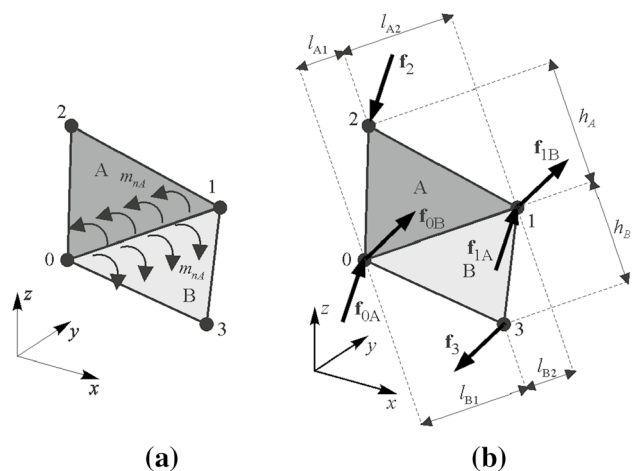
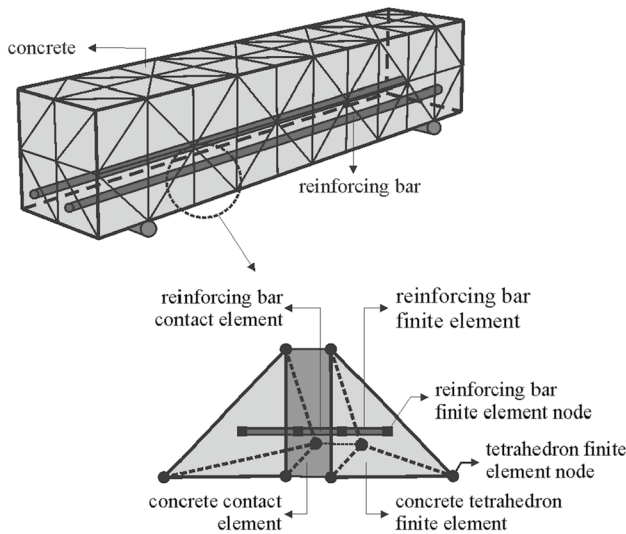


Fig. 10 Bending moment along the corresponding side of the observed finite element (a) and equivalent nodal forces due to bending moment (b)



**Fig. 11** Discretisation of reinforced concrete structures

within the uncracked concrete assuming the linear elastic behaviour of the reinforcing bar in the concrete finite element and a perfect bond between the concrete and the reinforcing bar, which means that the deformation of the concrete finite element influences the deformation of the reinforcing bar finite element. The axial forces in the reinforcing bar finite element nodes due to the deformation of the reinforcing bar finite element are transferred onto the nodes of the concrete finite elements in the form of equivalent nodal forces.

The behaviour of the reinforcing bar within the crack surface, which occurs upon reaching the tensile strength of the concrete, is modelled with the reinforcing bar contact elements by a non-dimensional slip  $s$  given by:

$$s = \left(\frac{S}{D}\right)K_{fc}, \quad K_{fc} = \left(\frac{f_c}{20}\right)^{2/3} \tag{25}$$

where  $S$  is the local slip of the bar from the crack interface (see Fig. 12a),  $D$  is the diameter of the bar, while  $f_c$  is the concrete compressive strength in (MPa). Considering the

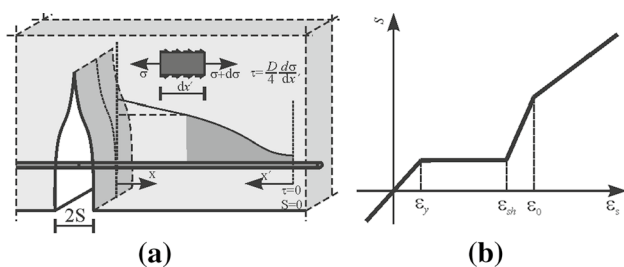


**Fig. 12** **a** Definition of local slip; **b** strain–slip relation under monotonic loading

experimentally based relation between the non-dimensional slip  $s$  and the strain of the reinforcing bar in the crack  $\epsilon_s$  [18] shown in Fig. 12, it is possible to obtain the strain, which, considering the material model of steel, yields the stress in the reinforcing bar within the crack faces. In the proposed numerical model, the Kato’s model [19] was adopted for defining the stress–strain relationship in the reinforcing bar. The forces in the reinforcing bar finite element nodes resulting from the stress in the reinforcing bar contact element are transferred onto the nodes of the concrete finite elements in the form of equivalent nodal forces.

Detailed information related to the numerical model of the reinforcing bar within FDEM can be found in [15–17].

### 2.8 Brick masonry structures in FDEM

For the purpose of analysing the masonry structures with mortar joints [20], the original Y-FDEM programme package was extended with a constitutive model in the brick finite elements considering the orthotropic behaviour, failure and softening in compression, which is especially pronounced in masonry structures with perforated bricks, and with the material model in joint elements simulating mortar joints and unit-mortar interface.

The elliptical hardening followed by the parabolic/exponential softening law in compression, as shown in Fig. 13, is considered in the finite elements for both material axes, with different compressive fracture energies  $G_{fc_i}$  and different compressive strengths  $f_{c_i}$ , where subscript  $i$  refers to the material axes corresponding to global axes  $x$  and  $y$ .

The material model in joint elements accounts for the decrease in the friction coefficient due to the increasing shear displacement, cyclic behaviour and the increase in the fracture energy in shear due to the increasing pre-compression stress according to the equation:

$$G_{f_i}^{II} = G_{f_0}^{II} - 106.31 \sigma \quad (\text{N/m}) \tag{26}$$

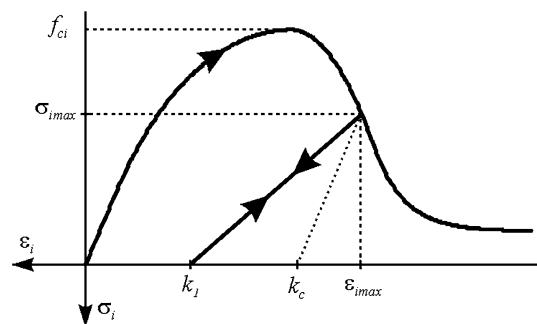


**Fig. 13** Hardening/softening law for compression with cyclic behaviour

where  $G_{f0}^H$  is the value of the fracture energy in shear without the normal pre-compression stress, while  $\sigma$  is the pre-compression stress in MPa.

The material model in joint elements fits rather well with the experimental results related to the behaviour of the unit-mortar interface in direct and cyclic tension and shear as shown in Figs. 14 and 15, respectively.

### 3 Some examples of FDEM simulations in structural engineering

This section presents a series of examples demonstrating the application of FDEM in the analysis of dry-joint masonry structures, concrete and reinforced concrete structures, masonry structures with mortar joints and confined masonry structures, cable and truss structures, membrane structures, plate and shell structures.

*Trusses and cable structures* The following example demonstrates the application of FDEM in the dynamic analysis of a space truss tower laterally secured with 12 prestressed

cables placed in four levels, with three cables at each level [9] as shown in Fig. 16a. The truss tower is 35 m high with an equilateral triangular body and 150 cm long in the ground plane. The chord of the truss is a tubular cross section with a 139.7 mm diameter and 8 mm thickness, while the diagonal and horizontal infill of the truss is also a tube cross section with a 60.3 mm diameter and 4 mm thickness. The cables are steel circular cross sections with a 20 mm diameter. The topmost level and the following level cables have the pre-tensioning force of 10 kN, the third level ones have the force of 35 kN, while the bottommost level ones have the pre-tensioning force of 40 kN. The anchors for the stay cable are 5 m away from the centre of the truss. The geometry of the combined truss and the cable structure was described with 1167 two-noded finite elements. The material of the structure is structural steel with the modulus of elasticity  $E = 210$  GPa and the mass per unit volume of  $7850$  kg/m<sup>3</sup>.

The structure was loaded with a uniform wind speed of 49.2 m/s at the full height of the column. Wind force acting on the truss elements and cables was obtained by using the force coefficients for the circular tubes. The force on

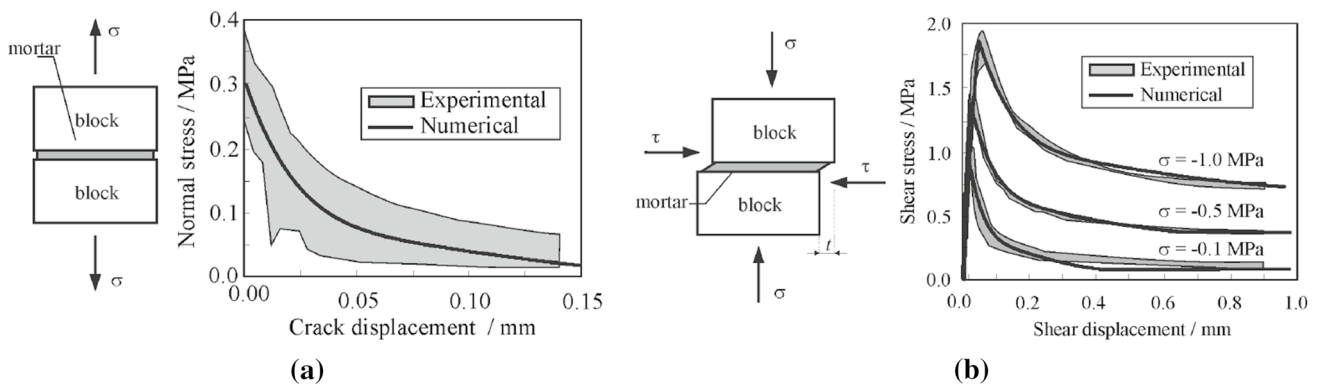


**Fig. 14** Numerical results in comparison with the experimental behaviour of unit-mortar interface in: **a** direct tension [21] for  $f_s = 0.30$  MPa,  $G_f^H = 12$  N/m and **b** direct shear [22] for  $f_s = 0.87$  MPa,  $\mu_0 = 1.01$ ,  $\mu_r = 0.73$

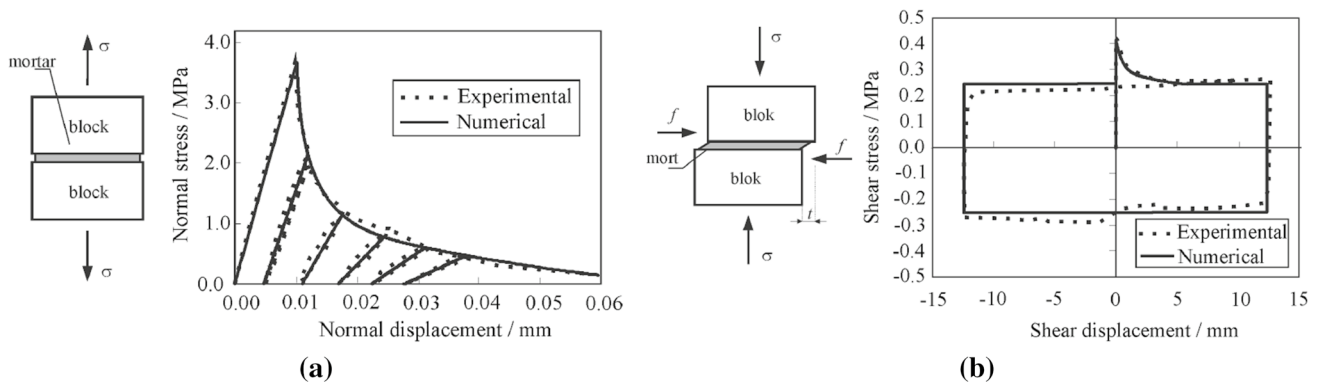


**Fig. 15** Numerical results in comparison with the experimental behaviour of unit-mortar interface in: **a** cyclic tension [23] for  $f_s = 0.36$  MPa,  $G_f^H = 100$  N/m and **b** cyclic shear [24] for  $f_s = 0.17$  MPa,  $G_f^H = 147$  N/m and  $\mu_0 = \mu_r = 0.70$

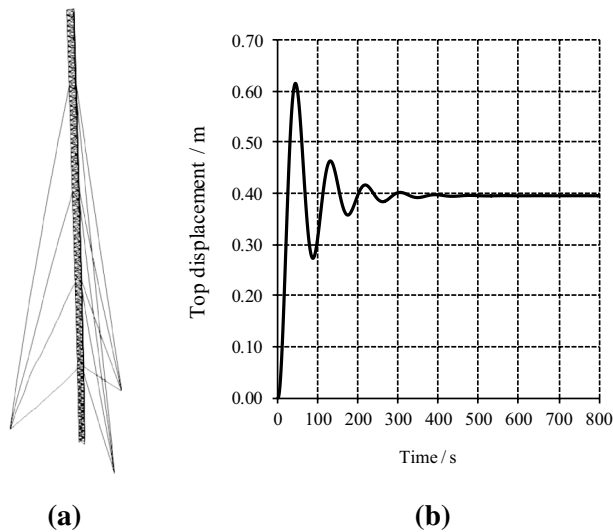


**Fig. 16** **a** Truss tower secured with cables; **b** horizontal displacement of the top in time

the belts was 700 N/m and 54 N/m by the cables. The wind force on the antenna mounted at 25 m from the ground was 1000 N, while the wind force on the antenna at the top of the truss was 6000 N. Antenna is modelled as an additional surface powered by the wind force.

Figure 16b shows the horizontal oscillations of the top of the truss tower in time up to achieving the state of rest due to the aeroelastic damping force. The results obtained by the presented FDEM numerical model were compared to the results obtained by the commercial software ROBOT. In the FDEM numerical model, the largest displacement occurring in the system is in the middle of the second level of the cable and is equal to 42.9 cm. The displacement of the top of the truss tower was 39.6 cm, which is 2% less in comparison with the ROBOT, while

the highest cable force was 77.5 kN, which is 3% less in comparison with the cable force obtained by ROBOT.

**Beam-type structures** The performance of the FDEM numerical model in the dynamic analysis of beam-type structures was presented on a simple supported beam with hinged and clamped boundary condition subjected to gravity load [10] as shown in Fig. 17. The beam end was assigned with the modulus of elasticity  $E=210$  GPa and the density of  $\rho=7850$  kg/m<sup>3</sup>. The width and the height of the cross section were adopted in the amount of 1 m and 0.01 m, respectively. For the purpose of the numerical analysis, the beam was discretised with 16 finite elements. Figure 17 shows the dynamic behaviour of the beam obtained by FDEM compared to the numerical solutions from ABAQUS where a rather good agreement of the results is obtained for both beams. In ABAQUS, beams were discretised by using 100 three-noded quadratic beam finite elements.

The application of the numerical model in the stability analysis and the behaviour of the structure after reaching the critical force were demonstrated on a simple supported and clamped arch structure subjected to a monotonically increasing displacement at their midspan, as shown in Fig. 18. Arch was assigned with the modulus of elasticity  $E=210$  GPa, density of  $\rho=7850$  kg/m<sup>3</sup>, 1 m width of the cross section and 0.2 m thickness. Geometry was discretised with 128 finite elements. Figure 18 shows the geometry of the arch and midspan deflections obtained by the FDEM numerical model compared to those obtained by ABAQUS, where a rather good agreement of the results can be observed. The numerical solutions from ABAQUS were obtained by using 244 three-noded quadratic beam finite elements.

**Membrane structures** The following example demonstrates the application of the FDEM numerical model in the analysis of the fracture pattern of the membrane exposed to tensile load over two edges [9]. The overall membrane dimensions are 2 m by 2 m with a 0.1-m-radius circular opening. The geometry of the membrane is described

**Fig. 17** Problem description of the steel beam and midspan deflection in time for: **a** hinge edges and **b** clamped edges

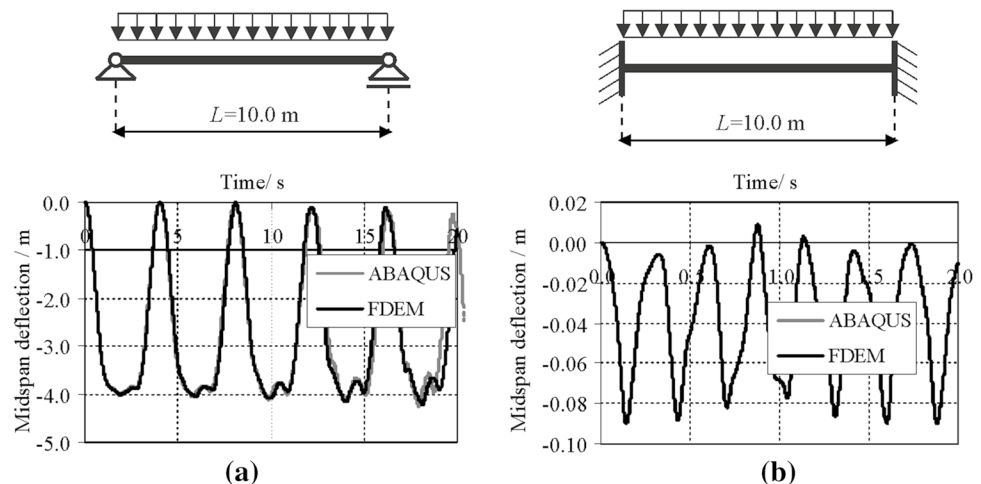
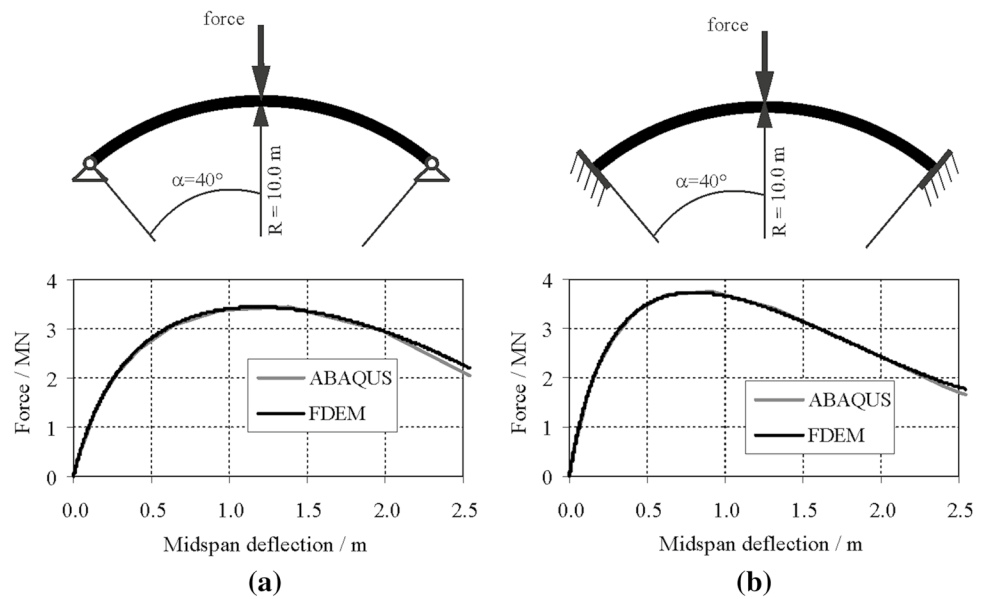




**Fig. 18** Problem description of the arch under point load and force–midspan deflection relation for: **a** hinge edges and **b** clamped edges



with 3072 finite elements. The membrane material was poly(methyl methacrylate), also known as the acrylic glass with a thickness of 0.5 mm and the modulus of elasticity  $E = 3.15\text{ GPa}$ . The ultimate tensile strength of the material equalled 73 MPa with the fracture energy of 310 J/m<sup>2</sup>. The stress is introduced as the stretching of the membrane by constant velocity displacement of 0.1 m/s of both the top and the bottom sides of the membrane. The fracture pattern of the membrane in time is shown in Fig. 19.

In addition, FDEM was applied to the analysis of the membrane wrinkling [9], which is manifested in local instabilities due to compression loading in the membrane.

For that purpose, a circular hollow membrane with a 60 cm outer diameter, 10 cm inner diameter and 0.18 cm thickness was adopted. Polyvinyl chloride (PVC) with the modulus of elasticity  $E = 5.56\text{ GPa}$  and the shear modulus

$G = 2.22\text{ GPa}$  was used as the membrane material. The geometry of the membrane is described by 12,480 finite elements. The membrane is preloaded with the mean radial stress of 766 N/m. The outer rim of the membrane was fixed, while the internal border was displaced with a constant angular speed of 0.016 rad/s. As in the physical experiment, the first wrinkling was observed at a torque of 15.7 Nm in the inner ring. Figure 20 presents the experimental [25] and numerical displacement field at a torque of 39.2 Nm, where a rather good agreement of results can be observed.

*Plate and shell structures* The performance of the FDEM numerical model in the analysis of shell structures with a highlighted geometric nonlinearity was demonstrated on a hinged cylindrical roof subjected to the central pinching force [20] as shown in Fig. 21a. The cylindrical roof has the modulus of elasticity  $E = 3102.75\text{ N/m}^2$ , Poisson’s ratio

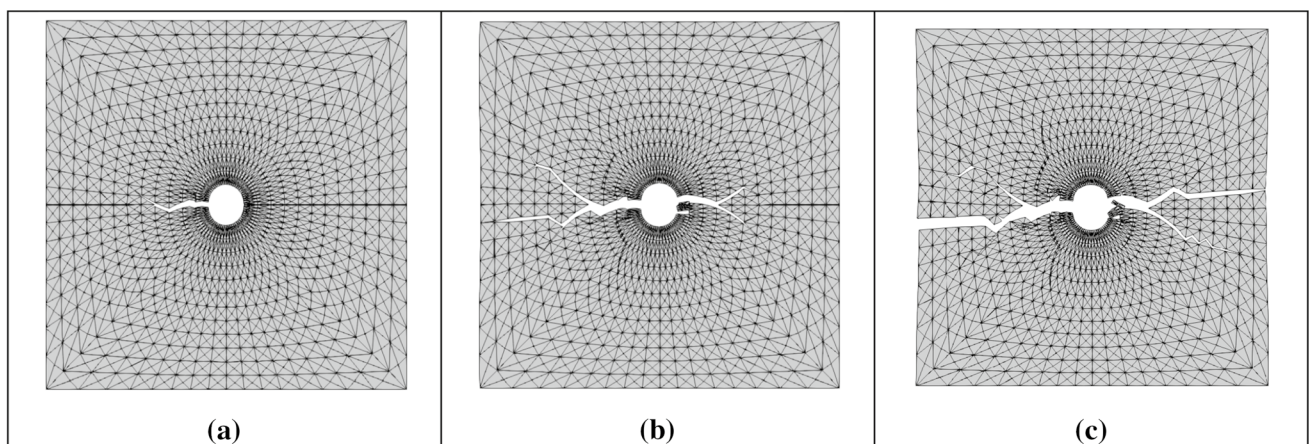


**Fig. 19** Membrane exposed to tensile load over two edges in time of: **a**  $t = 1.05\text{ s}$ ; **b** 1.08 s and **c**  $t = 1.1\text{ s}$

**Fig. 20** Membrane wrinkling: **a** experimental results [25]; **b** numerical results

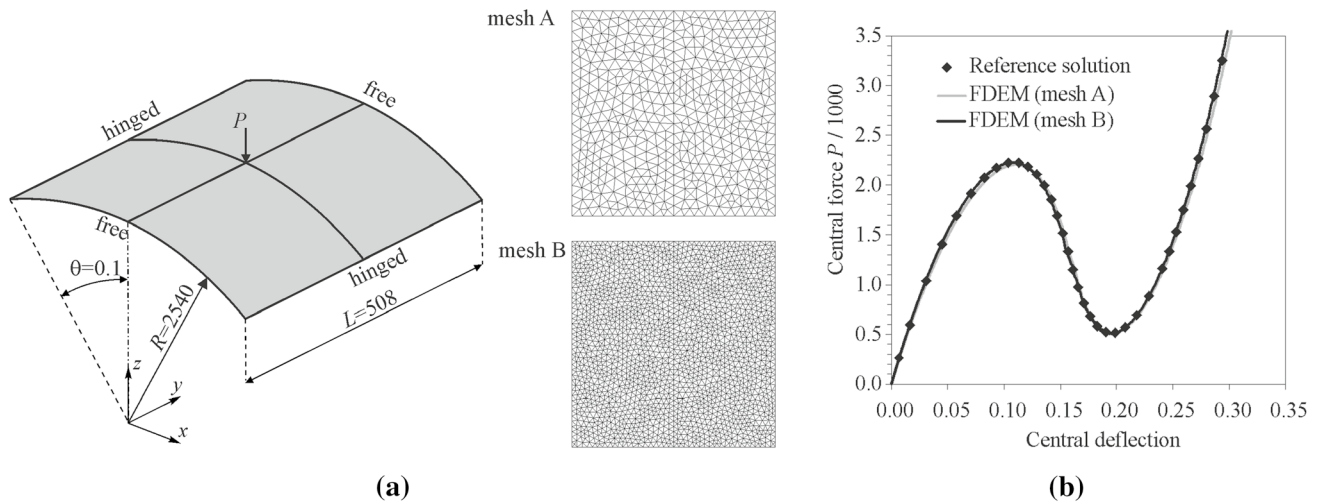
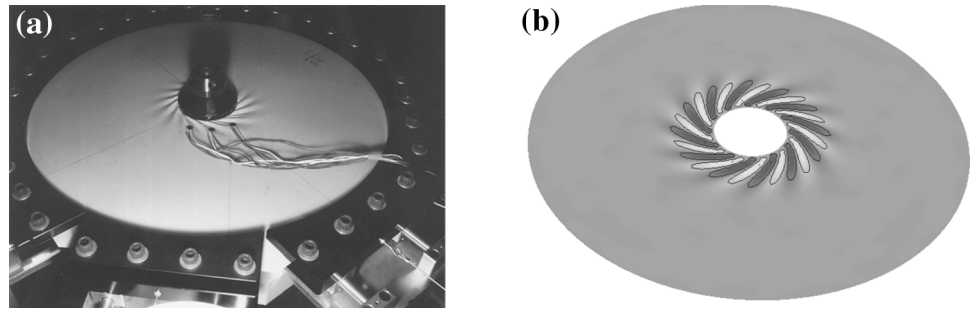


**Fig. 21** Hinged cylindrical roof subjected to the central pinching force: **a** problem description and meshes used for the numerical analysis; **b** load–deflection curves

$\nu=0.3$  and thickness of 12.7 m. Geometry was described with 962 (Mesh A) and 3710 (Mesh B) finite elements. Figure 21b shows the comparison of numerical solution obtained by the FDEM numerical model with a reference solution obtained with the programme package ABAQUS by using 1024 S4R finite elements. The results show excellent correspondence for both mesh refinements.

Another example [13] demonstrates a large rotation capability of the FDEM numerical model. For that purpose, a 12-m-long, 1-m-wide and 0.1-m-thick cantilever plate was subjected to different moments at the unrestrained end. Geometry was described with  $24 \times 4$  and  $48 \times 4$  finite elements. The cantilever has the modulus of elasticity  $E = 1.2 \times 10^6 \text{ N/m}^2$  and Poisson's ratio  $\nu = 0$ . Figure 22a shows the comparison of the numerical and analytical results for the vertical tip deflection and the horizontal tip deflection, where a rather good agreement of the results can be observed for both finite element meshes, while Fig. 22b shows a deformed  $48 \times 4$  mesh for different end moments.

In order to demonstrate the application of FDEM in the stability analysis of shell structures, a cylindrical shell was exposed to the compression stress at unrestrained

ends via the displacement at the top of the shell. The velocity of the displacement was proportional to time  $t$  as  $v = 2.27t \times 10^{-5} \text{ m/s}$ . The cylinder has the modulus of elasticity  $E = 210 \text{ GPa}$ , Poisson's ratio  $\nu = 0.3$ , 1 m radius, 3 m height and 5 mm thickness. Geometry was discretised with 3922 finite elements. Figure 23 shows the form of stability loss of the cylindrical shell in different moments.

*Concrete and reinforced concrete structures* The following example demonstrates the application of FDEM in the analysis of concrete and reinforced concrete beams exposed to impact loading. The problem description and finite element mesh used in the analysis are presented in Fig. 24a, b, respectively. The missile mass and initial velocity equalled 37.5 kg and 80 m/s, respectively. The impact was analysed for the case of a beam without the reinforcement and for the beam reinforced with a longitudinal reinforcing bar and stirrups. Material characteristics of the concrete and the reinforcement used in the analysis are presented in Table 1.

Figures 25 and 26 show the crack patterns in different times in the concrete and reinforced concrete beams, respectively.

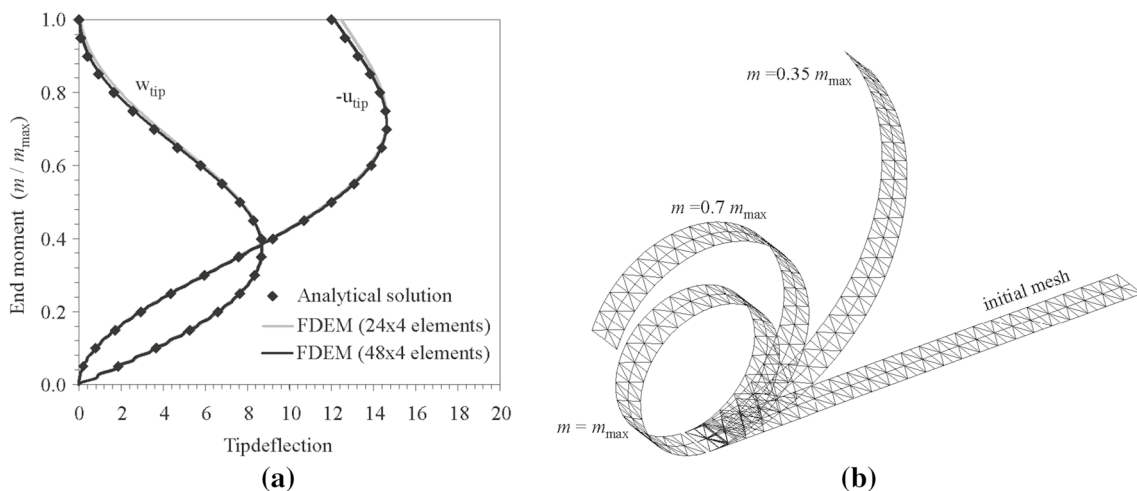


Fig. 22 Cantilever plate subjected to end moment. a Load–deflection curves. b The deformed 48 × 4 mesh under the moment

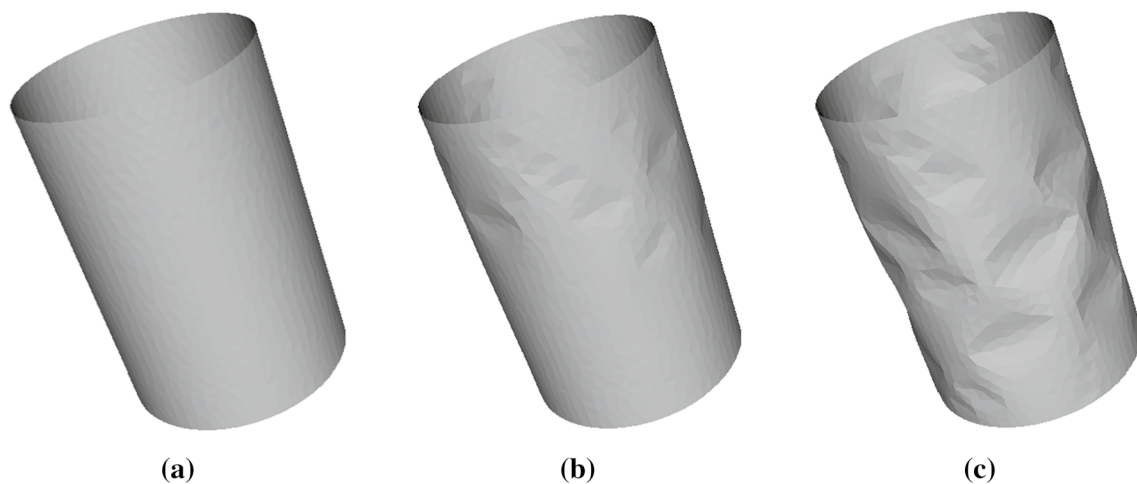


Fig. 23 Cylindrical shell under compression load over the free edges in time a 10 s; b 21 s and c 40 s

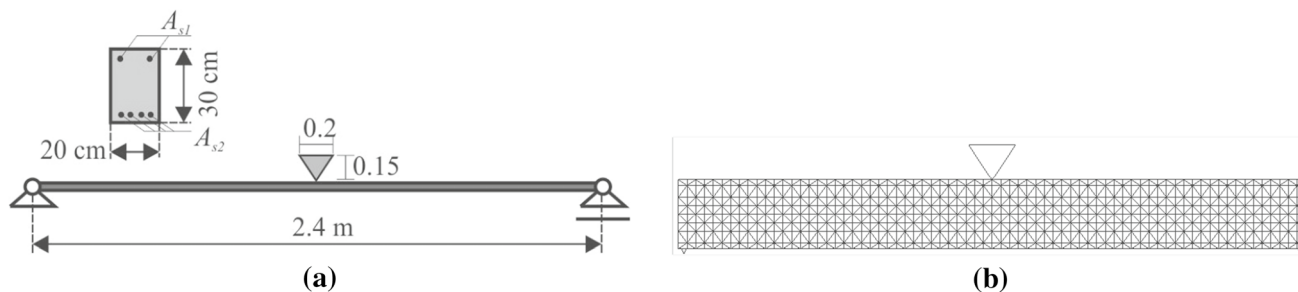


Fig. 24 a Geometry characteristics of reinforced concrete beam; b discretisation of beam

The ability of the model to simulate the structural response under cyclic loading conditions was presented on the reinforced concrete beam [15, 16] (see Fig. 28a) which was experimentally tested by Maekawa [18] et al. The

modulus of elasticity and the compressive strength of the concrete equalled 29 GPa and 29 MPa, respectively, while the reinforcement had the modulus of elasticity of 190 GPa, yielded the stress of 350 MPa, ultimate stress of 540 MPa,

**Table 1** Material characteristics of the concrete and the reinforcement

Concrete		Steel	
$E_c$ /MPa	29,730	$E_s$ /MPa	210 000
$N$	0.2	$f_y$ /MPa	420
$f_t$ /MPa	3.12	$A_{s1}$ /cm <sup>2</sup>	1.02
$f_c$ /MPa	40	$A_{s2}$ /cm <sup>2</sup>	4.52
		Stirrups	$\phi$ 8/15 cm

strain at the onset of hardening of 0.0165, ultimate strain of 0.1 and the strain at the fracture of 0.019. Figure 27a shows the comparison of experimental and numerical results of

the reinforced concrete beam exposed to cyclic tensile loading where a rather good agreement can be observed, while Fig. 27b, c shows the crack pattern obtained with the FDEM numerical model for coarse and fine finite element meshes, respectively.

*Brick masonry with mortar joints and confined masonry walls* The performance of the FDEM numerical model in the analysis of a masonry structure was demonstrated on the masonry shear wall exposed to monotonically increasing lateral loading. The experimental testing of the wall was conducted by Rajmakers and Vermeltoort [26].

The wall had a width/height ratio of 990 mm/1000 mm and consisted of 18 rows of blocks. The wall was made of

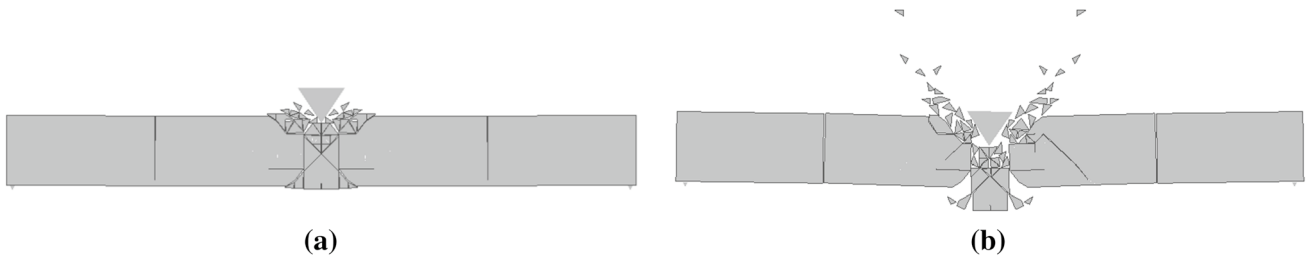


**Fig. 25** Concrete beam exposed to missile impact in time: **a**  $t = 1.0$  ms and **b**  $t = 5.0$  ms

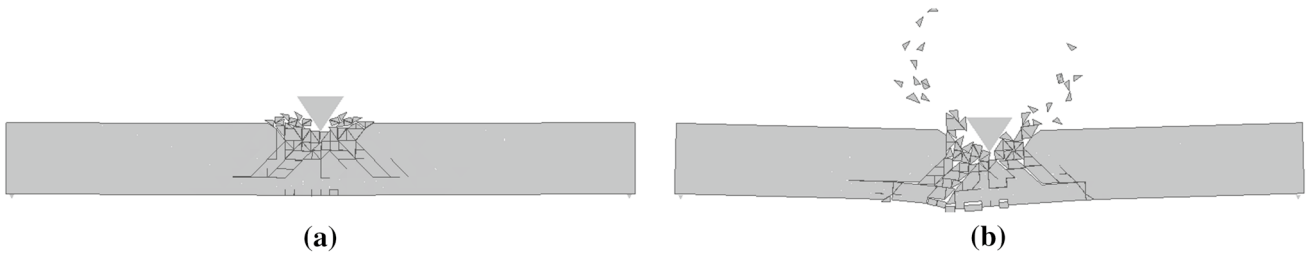
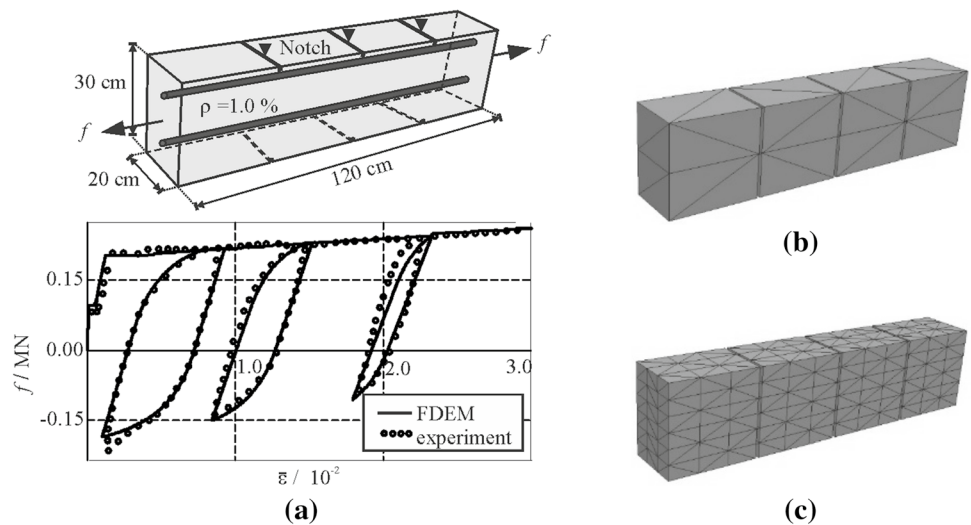


**Fig. 26** Reinforced concrete beam exposed to missile impact in time: **a**  $t = 1.0$  ms and **b**  $t = 5.0$  ms

**Fig. 27** Reinforced concrete beam exposed to tensile cyclic load: **a** geometry and loading history; **b** crack pattern for coarse finite element mesh and **c** crack pattern for fine finite element mesh



solid clay bricks with the dimensions of 210×98×50 mm and 10-mm-thick mortar. After applying the pre-compression stresses in the amount of 1.21 MPa, the wall was subjected to the horizontal load, which was achieved through the controlled displacement of the steel beam at the top of the wall. The loading rate was  $12 \times 10^{-6}$  m/s. The mechanical characteristics of materials used in the numerical analysis are based on the data taken from the literature [26] and shown in Table 2.

Figure 28 shows the behaviour of the wall after collapse. This example highlights the ability of a combined FEM/DEM in simulating the behaviour of the structure after reaching the ultimate load which can be important in analysing the progressive collapse of the structure.

The combination of the material model for the brick masonry with the material model for the reinforced concrete structures enables the analysis of confined masonry walls whose application was demonstrated on the example of a two-storey wall exposed to a gradually increasing seismic loading until collapse [20]. Geometry and discretisation of the confined masonry wall are shown in Fig. 29. Wall thickness equalled 0.25 m.

**Table 2** Material characteristics of materials

Unit	Interface element		
$E_x/E_y$	7520	$f_t$	0.16
MPa	3960	MPa	
$f_{cx}/f_{cy}$	10.5	$f_s$	0.224
MPa	10.5	MPa	
$f'_f/f_s$	2.0	$G_f^I$	18
MPa	2.8	N/m	
$G_f^I / G_f^II$	80	$G_f^II$	50
N/m	500	N/m	
$G_{fcx} / G_{fcy}$	20,000	$\mu_0 = \mu_r$	0.75
N/m	15,000		

Material characteristics of the wall are presented in Tables 3 and 4. Vertical load of 0.5 MPa was applied to the horizontal reinforced confining elements of each storey. The wall was exposed to the horizontal ground acceleration recorded on April 15, 1979, in Dubrovnik on rock soil during an earthquake with the epicentre in Petrovac (Montenegro). Figure 30 shows the crack pattern in the confined masonry wall exposed to earthquake loading with a pickup acceleration of  $a_g = 4.0$  m/s<sup>2</sup> in time.

*Dry-joint masonry structures* Due to its discontinuous nature, FDEM proved to be rather suitable for the analysis of dry-joint masonry structures where each block is observed as one discrete element [27–29]. The energy dissipation mechanisms due to dry friction and contact impact, implemented within the numerical algorithm for calculating contact forces, has yielded rather good results in the simulation of tangential friction forces between the blocks and the simulation of rocking motion of the block in comparison with the experimental results [27–29].

The following example presents the ability of FDEM to reproduce the mechanical behaviour and the failure mechanism of the brick masonry wall subjected to vertical in-plane loading. Numerical analysis was performed on single-leaf brickwork masonry walls CL1 tested by Bui et al. [30] in the laboratory. The arrangement of CL1 test panel is shown in Fig. 31a, while the discretisation of the wall used in the numerical analysis is shown in Fig. 31b. One part of the wall was supported on a fixed base, while the other part of the wall was supported on the base allowing vertical displacement. The test panel wall was constructed with 50 mm × 105 mm × 220 mm (height × span × breadth) bricks. The unit weight of the brick was 2200 kg/m<sup>3</sup>, while the angle of friction between the faces of bricks, which equalled 38°, was determined experimentally. The Young’s modulus and the Poisson’s ratio of the masonry block were adopted from the experimental analysis and equalled 9700 MPa and 0.2, respectively. The wall panel was tested under gravity load

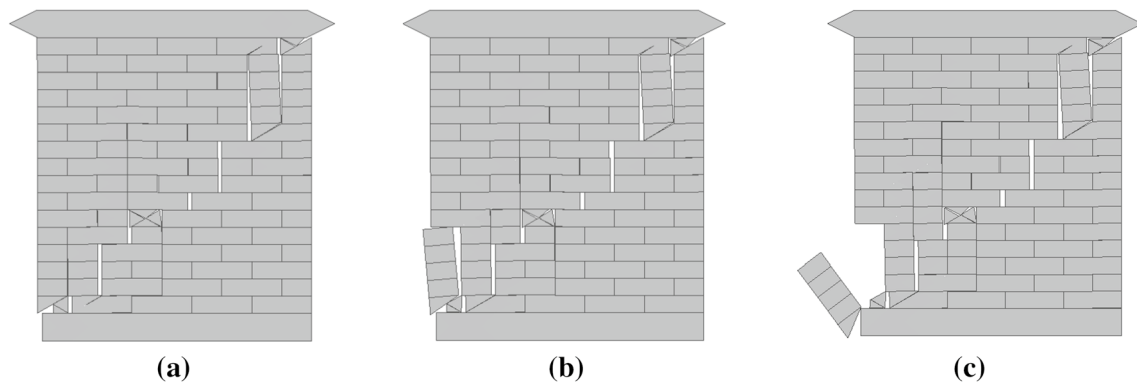


**Fig. 28** Collapse mechanism of the masonry wall exposed to lateral in-plane loading at displacement: **a**  $\delta=18$  mm, **b**  $\delta=21$  mm and **c**  $\delta=24$  mm

**Fig. 29** Geometry and discretisation of confined masonry wall

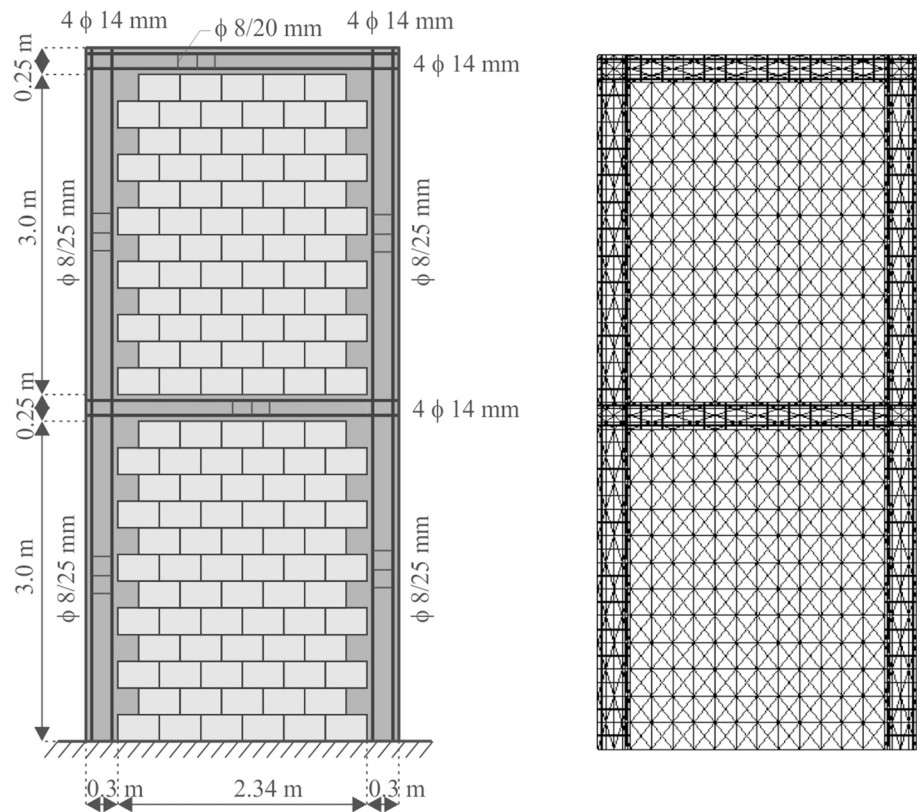


**Table 3** Material characteristics of reinforced concrete elements

Concrete		Steel	
$E_c$ /MPa	30,500	$E_s$ /MPa	2,10,000
$f_t$ /MPa	3.8	$f_y$ /MPa	500
$f_c$ /MPa	38.0	$f_u$ /MPa	650
$G_f$ (N/m)	150		

**Table 4** Material characteristics of unit and interface elements

Unit		Interface element	
$E_x = E_y$ /MPa	1033	$f_t$ /MPa	0.16
$\nu$	0.141	$f_s$ /MPa	0.224
$f_{cx}$ /MPa	2.7	$G_{if}$ (N/m)	12
$f_{cy}$ /MPa	10.33	$G_{is}$ (N/m)	50

and vertical deflection of the movable base. The settlement of the base was applied incrementally until the failure mechanism occurred. The failure mechanism is shown in Fig. 32 where a rather good agreement can be observed in comparison with the experimental results.

In order to demonstrate the performance of FDEM in reproducing the failure mechanism due to the coupled in-plane and out-of-plane behaviour, three connected

dry-stone masonry wall with the geometry shown in Fig. 33 were exposed to the horizontal monotonically increasing base acceleration given by  $a_{0x}(t)/g = \pm 0.02t$ . The width, height and thickness of the block used in the numerical analysis were 60 cm, 30 cm and  $b = 30$  cm, respectively, while the friction coefficient between the blocks was equal to 0.7. The discretisation of the walls is shown in Fig. 33b.

Figure 34 shows the failure mechanism of the walls for both the positive acceleration and the negative acceleration.

Y-FDEM programme package was also used as a basis for the implementation of the numerical model of metal clamps and bolts, and the seismic loading [29] which enables the estimation of seismic resistance of strengthened dry-stone masonry structures as presented in the example of the Prothyron structure within the Diocletian’s Palace in Split (see Fig. 35). The structure was exposed to horizontal and vertical ground acceleration recorded on April 15, 1979, in Dubrovnik on rock soil during an earthquake with the epicentre in Petrovac (Montenegro). Material characteristics of stone used in the numerical analysis include the tensile strength of 10 MPa, shear strength of 20 MPa, fracture energy in tension of 720 N/m and fracture energy in shear of 1440 N/m. Bolts were made of steel with the Young’s modulus of elasticity of 181,000 MPa and the tensile strength

**Fig. 30** Crack pattern in confined masonry wall exposed to earthquake loading with pickup acceleration of  $a_g = 4.0 \text{ m/s}^2$  at time: **a**  $t = 4.85 \text{ s}$ ; **b**  $t = 8.75 \text{ s}$ ; **c**  $t = 12.00 \text{ s}$

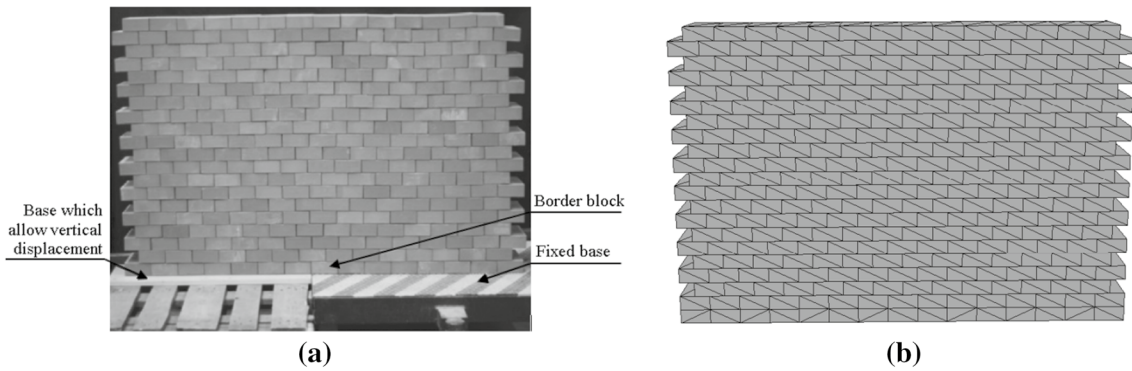
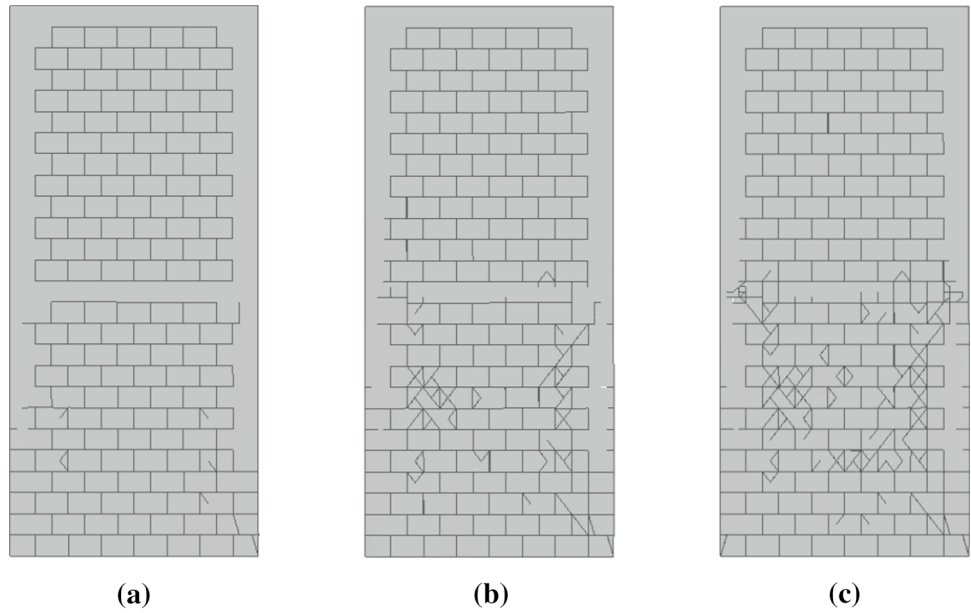
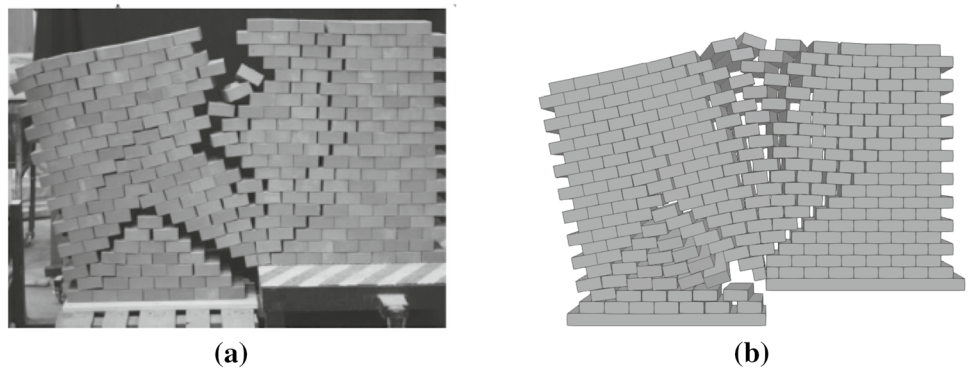


**Fig. 31** Test CL1: **a** configuration of the test [31] and **b** discretisation

**Fig. 32** Failure mechanism of in-plane loading masonry wall: **a** experimental; **b** numerical FDEM



of 414 MPa. The collapse mechanism for the dry stone structure with steel bolts and peak ground acceleration of  $a_g = 0.45 \text{ g}$  over time is shown in Fig. 36.

### 4 Conclusion

This paper demonstrates the application of FDEM in structural mechanics. Compared to the experimental results and

**Fig. 33** Three connected dry-stone masonry walls: **a** geometry and **b** discretisation

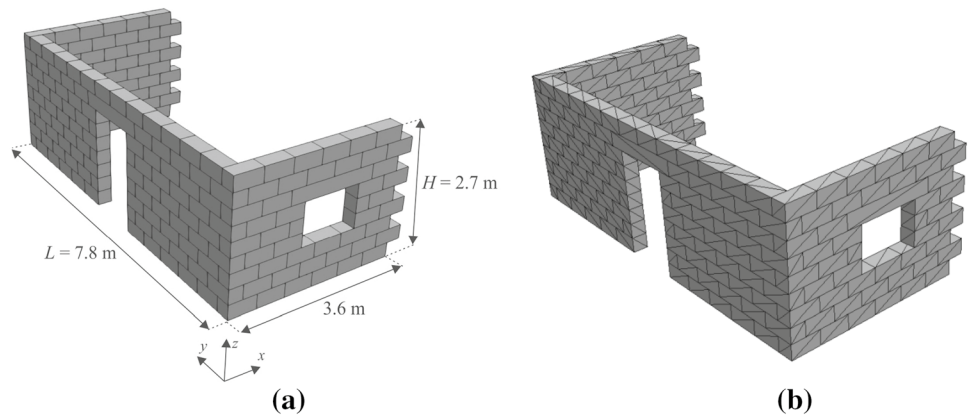


**Fig. 34** Failure mechanism of dry-stone masonry structure exposed to monotonically increasing lateral loading in: **a** positive direction; **b** negative direction

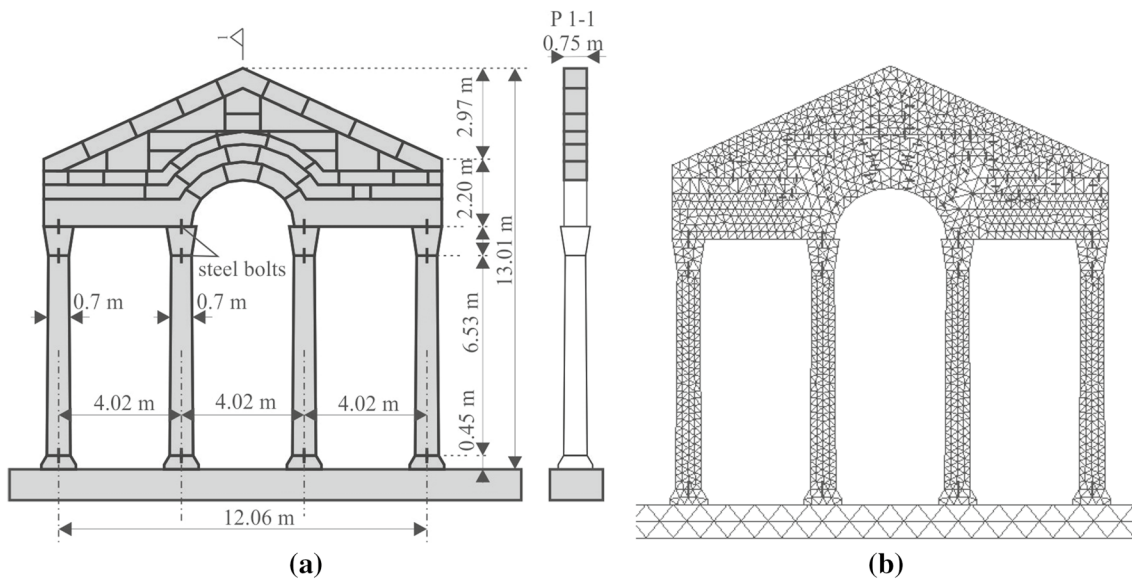
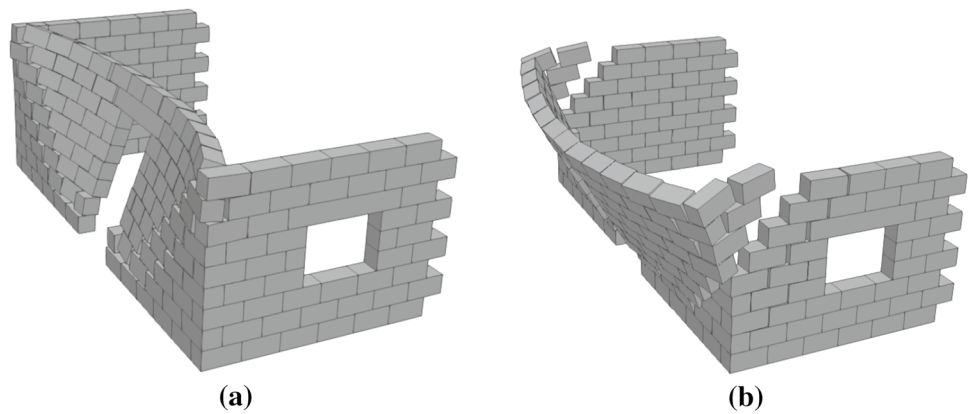


**Fig. 35** Prothyron structure: **a** geometry and **b** discretisation

due to its simplicity based on the explicit presentation of the equation of motion, taking into account large rotations, large displacements and finite deformations, this method has shown to be promising in the analysis of various types

of structural systems such as dry-joint masonry structures, concrete and reinforced concrete structures, masonry structures with mortar joints, confined masonry structures,



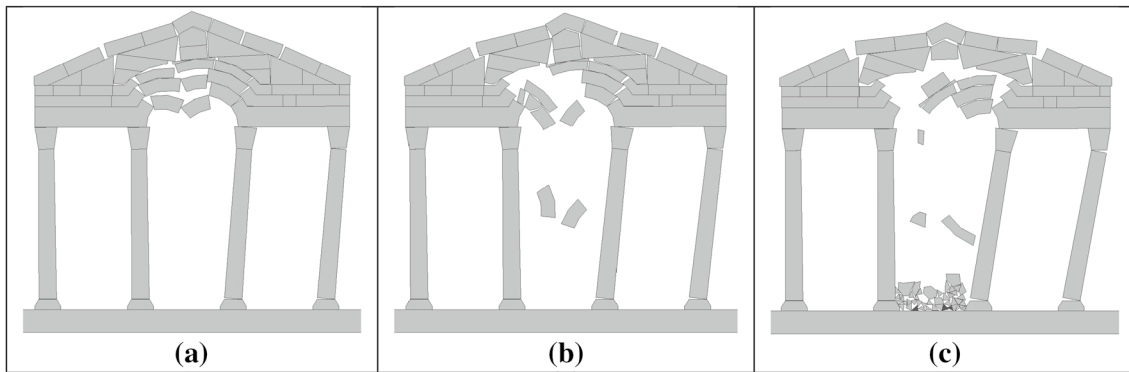


**Fig. 36** Collapse mechanism of Prothyron structure with steel bolts exposed to earthquake loading in time: **a**  $t = 17.9$  s; **b**  $t = 18.7$  s; **c**  $t = 19.6$  s

cable and truss structures, membrane structures, plate and shell structures.

In the follow-up to the recent research, FDEM is to be applied for geotechnical analysis, including the stability analysis combined with the dynamic loads and with paired gravitational and earthquake loads. In addition, the application of FDEM in the analysis of the laminar fluid flow and in the interaction of fluid with the structures is yet to be tested. Special emphasis will be attributed to shock waves caused by sudden dynamic loads, such as earthquakes and underwater explosions. Other objectives include the extensions of the existing algorithms for the analysis of beam, plate and shell structures in order to account for the material nonlinearity, thus enabling the analysis of the 3D frames released from the rotational degrees of freedom.

**Acknowledgements** This paper is supported by the Croatian Science Foundation under the project *Development of numerical models for reinforced-concrete and stone masonry structures under seismic loading based on discrete cracks* (IP-2014-09-2319) and by the Croatian Government and the European Union through the European Regional Development Fund—the Competitiveness and Cohesion Operational Programme under the Project KK.01.1.1.02.0027.

## References

- Munjiza A (2004) The combined finite-discrete element method. Wiley, London
- Munjiza A, Andrews KRF (1998) NBS contact detection algorithm for bodies of similar size. *Int J Numer Meth Eng* 43(1):131–149. [https://doi.org/10.1002/\(SICI\)1097-0207\(19980915\)43:1%3C131:AID-NME447%3E3.0.CO;2-S](https://doi.org/10.1002/(SICI)1097-0207(19980915)43:1%3C131:AID-NME447%3E3.0.CO;2-S)
- Munjiza A, Andrews KRF (2000) Penalty function method for combined finite-discrete element system comprising large number of separate bodies. *Int J Numer Meth Eng* 49(11):1377–1396. [https://doi.org/10.1002/1097-0207\(20001220\)49:11%3C1377:AID-NME487%3E3.0.CO;2-A](https://doi.org/10.1002/1097-0207(20001220)49:11%3C1377:AID-NME487%3E3.0.CO;2-A)
- Smoljanović H, Živaljić N, Nikolić Ž, Munjiza A (2018) Numerical analysis of 3D dry-stone masonry structures by combined finite-discrete element method. *Int J Sol Struct* 136–137:150–167. <https://doi.org/10.1016/j.ijsolstr.2017.12.012>
- Munjiza A, Andrews KRF, White JK (1998) Combined single and smeared crack model in combined finite-discrete element method. *Int J Numer Meth Eng* 44(1):41–57. [https://doi.org/10.1002/\(SICI\)1097-0207\(19990110\)44:1%3C41:AID-NME487%3E3.0.CO;2-A](https://doi.org/10.1002/(SICI)1097-0207(19990110)44:1%3C41:AID-NME487%3E3.0.CO;2-A)
- Munjiza A, John NWM (2002) Mesh size sensitivity of the combined FEM/DEM fracture and fragmentation algorithms. *Eng Fract Mech* 69:281–295. [https://doi.org/10.1016/S0013-7944\(01\)00090-X](https://doi.org/10.1016/S0013-7944(01)00090-X)
- Munjiza A, Knight EE, Rouiger E (2012) Computational mechanics of discontinua. Wiley, London
- Munjiza A, Owen DRJ, Bicanic N (1995) A combined finite-discrete element method in transient dynamics of fracturing solids. *Eng Comput* 12:145–174. <https://doi.org/10.1108/02644409510799532>
- Divić V (2014) Simulations of ultimate limit states under wind loading by combined finite discrete element method. Dissertation (in Croatian), University of Split, Croatia
- Smoljanović H, Uzelac I, Trogrlić B, Živaljić N, Munjiza A (2018) A computationally efficient numerical model for a dynamic analysis of beam type structures based on the combined finite discrete element method. *MatWerk* 49(5):651–665. <https://doi.org/10.1002/mawe.201700277>
- Divić V, Uzelac I, Peroš B (2014) Multiplicative decomposition based fdem model for membrane structures. *Trans FAMENA* 38:1–12
- Uzelac I, Smoljanović H, Peroš B (2015) A computationally efficient numerical model for a dynamic analysis of thin plates based on the combined finite–discrete element method. *Eng Struct* 101:509–517. <https://doi.org/10.1016/j.engstruct.2015.07.054>
- Uzelac I, Glavinić I, Smoljanović H, Galić M, Munjiza A, Mihanović A (2018) Computational aspects of the combined finite- discrete element method in static and dynamic analysis of shell structures. *MatWerk* 49(5):635–651. <https://doi.org/10.1002/mawe.201700276>
- Uzelac I, Smoljanovic H, Batinic M, Peroš B, Munjiza A (2018) A model for thin shells in the combined finite- discrete element method. *Eng Comput* 35(1):377–394. <https://doi.org/10.1108/EC-09-2016-0338>
- Živaljić N, Smoljanović H, Nikolić Ž (2013) A combined finite-discrete element model for RC structures under dynamic loading. *Eng Comput* 30(7):982–1010. <https://doi.org/10.1108/EC-03-2012-0066>
- Živaljić N, Nikolić Ž, Smoljanović H (2014) Computational aspects of the combined finite—discrete element method in modelling of plane reinforced concrete structures. *Eng Fract Mech* 131:669–686. <https://doi.org/10.1016/j.engfracmech.2014.10.017>

17. Nikolić Ž, Živaljić N, Smoljanović H, Balić I (2017) Numerical modelling of reinforced-concrete structures under seismic loading based on the finite element method with discrete interelement cracks. *Earth Eng Struct Dyn* 46(1):159–178. <https://doi.org/10.1002/eqe.2780>
18. Maekawa K, Pimanmas A, Okamura, H (2003), *Nonlinear mechanics of reinforced concrete*, London
19. Kato B (1979) Mechanical properties of steel under load cycles idealizing seismic action. In: *Bulletin D'Information 131*, CEB, AICAP-CEB symposium, Rome pp 7–27
20. Smoljanović H, Nikolić Ž, Živaljić N (2015) A combined finite-discrete numerical model for analysis of masonry structures. *Eng Fract Mech* 136:1–14. <https://doi.org/10.1016/j.engfracmech.2015.02.006>
21. Van der Pluijm R (1992) Material properties of masonry and its components under tension and shear. In: Neis VV (ed) *Canadian masonry symposium: proceedings of the 6th Canadian masonry symposium*, Saskatoon, Saskatchewan pp 675–686
22. Van der Pluijm R (1993) Shear behaviour of bed joints. In: Hanid AA, Harris HG (ed) *North American masonry conference: proceedings of the 6th North American Masonry Conference*, Philadelphia, Pennsylvania, pp 125–136
23. Gopalaratnam VS, Shah SP (1985) Softening response of plain concrete in direct tension. *ACI J* 82:310–323. <https://doi.org/10.14359/10338>
24. Atkinson RH, Amadei BP, Saeb S, Sture S (1989) Response of masonry bed joints in direct shear. *J Struct Eng* 115(9):2276–2296
25. Miyamura T (2000) Wrinkling on stretched circular membrane under in-plane torsion: bifurcation analyses and experiments. *Eng Struct* 22(11):1407–1425
26. Raijmakers TMJ, Vermeltoort AT (1992) Deformation controlled tests in masonry shear walls. Delft, TNO-Bouw, Report No. B-92-1156
27. Smoljanović H, Živaljić N, Nikolić Ž (2013) A combined finite-discrete element analysis of dry stone masonry structures. *Eng Struct* 52:89–100. <https://doi.org/10.1016/j.engstruct.2013.02.010>
28. Balić I, Živaljić N, Smoljanović H, Trogrlić B (2016) Seismic resistance of dry stone arches under in-plane seismic loading. *Struct Eng Mech* 58(2):243–257. <https://doi.org/10.12989/sem.2016.58.2.243>
29. Smoljanović H, Nikolić Ž, Živaljić N (2015) A finite-discrete element model for dry stone masonry structures strengthened with steel clamps and bolts. *Eng Struct* 90:117–129. <https://doi.org/10.1016/j.engstruct.2015.02.004>
30. Bui T, Limam A, Sarhosis V, Hjjaj M (2017) Discrete element modelling of the in-plane and out-of-plane behaviour of dry-joint masonry wall constructions. *Eng Struct* 136(1):277–294. <https://doi.org/10.1016/j.engstruct.2017.01.020>

**Publisher's Note** Springer Nature remains neutral with regard to jurisdictional claims in published maps and institutional affiliations.